Article:
He, Y, Bayly, AE orcid.org/0000-0001-6354-9015, Hassanpour, A orcid.org/0000-0002-7756-1506 et al. (2 more authors) (2020) Flow behaviour of an agitated tubular reactor using a novel dynamic mesh based CFD model. Chemical Engineering Science, 212. 115333. ISSN 0009-2509

https://doi.org/10.1016/j.ces.2019.115333

Flow behaviour of an agitated tubular reactor using a novel dynamic mesh based CFD model

Yi He*, Andrew E. Bayly, Ali Hassanpour, Michael Fairweather, Frans Muller
School of Chemical and Process Engineering, University of Leeds, Leeds, LS2 9JT, UK

Abstract

Agitated tubular reactor (ATR) is an intensified, continuous, reactor design in which radial mixing is decoupled from axial flow. This study proposed a new CFD approach to study fluid dynamics and mixing mechanisms in the ATR. It combines a soft-sphere collision model with a dynamic meshing approach on ANSYS Fluent to tackle structure-structure and fluid-structure interactions (FSI) simultaneously. Its ability to handle FSI is validated on sedimentation of a large sphere in a quiescent fluid. A periodic motion of the agitator was predicted, which is mainly driven by contact with the external oscillating tube. The fluid motion is complex, with vortex structures forming behind the agitator at its highest point and the highest fluid velocities seen as fluid is squeezed under the agitator. Performance of Reynolds stress models were evaluated and pressure-strain term shows little effect on agitator's motion. The energy was found to be mainly consumed by viscous dissipation.

Keywords: CFD; fluid-structure interaction; agitated tubular reactor; dynamic meshing approach; Reynolds stress model; process intensification;

* Corresponding author.
E-mail address: y.he1@leeds.ac.uk (Y. He)

1. Introduction

Flow reactors are widely used in chemical processing for various purposes, such as catalytic reaction, crystallization, polymerization, dispersing gases and solids (Bakker and Van Den Akker, 1994; David et al., 1991; Derksen, 2003, 2012; Jaisinghani and Ray, 1977). The focus of this study is given to a novel agitated tubular reactor, intensified for continuous chemical processing and is especially suitable for long residence time processes. The ATR system consists of up to ten reactor tubes connected in series and is mounted on a shaking platform. Each tube contains a free-moving internal agitator (Fig. 1). Unlike conventional mechanically agitated reactors, there are no drive shafts and baffles (Harvey et al., 2003; Ni et al., 2001). The motion of the agitator is driven by collision with the external tube due to lateral shaking of the reactor body, and is also affected by interactions with the fluid flow. Different designs of the agitator have been proposed, such as solid bar or perforated tube. Fig. 1 shows a cross-section of an operational unit of a typical ATR system. End caps are deliberately attached to the agitator to prevent direct contact with the tube surface such that the chances of milling of any catalyst particles can be reduced. The ATR system has many advantages, such as simple geometry and easy sealing. The capability of achieving radial mixing while maintaining an orderly axial flow makes it well suited for intensifying the handling of slurries, gas/liquid mixtures and catalysed reactions (Browne et al., 2011; Gasparini et al., 2012). To date, however, most of the studies on the ATR system have focused on their bulk performance, such as residence time characterisation, volumetric mass and heat transfer (Gasparini et al., 2012; Jones et al., 2012). Nevertheless, understanding of its mixing mechanism is still lacking, which hinders the development of general guidelines for design optimization and performance enhancement.

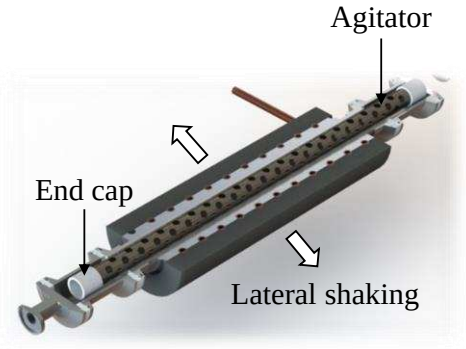

Fig. 1. Schematic of the cross-section of one unit of the reactor tube (courtesy AM Technology).

A large number of experimental and computational studies have highlighted the role of local flow structure in the mixing performance of mechanically agitated reactors (Hartmann et al., 2006; Kerdouss et al., 2006; Zadghaffari et al., 2009). Considerable experimental efforts have been devoted to measure the flow field using laser-Doppler velocimetry and particle image velocimetry (Pan et al., 2008; Rutherford et al., 1996; Zadghaffari et al., 2009). However, application of these techniques to the ATR system is still challenging due to the lateral shaking of the reactor body.

In recent years, computational fluid dynamics (CFD) has become a cost-effective alternative for studying chemical reactors, as it allows for a detailed understanding of physical phenomena occurring within the reactor and permits the development of correlations of value in equipment design. For example, turbulent stresses and energy dissipation are directly linked to the mixing performance and power consumption in such reactors. Nevertheless, application of CFD methods to the ATR system is not straightforward. One major question is how to deal with the free-moving internal agitator. In chemical reactor modelling, different approaches have been proposed to treat moving boundaries. For example, an impeller in a stirred tank can be handled using stationary boundary conditions (Brucato et al., 1998). Kresta and Wood (1991) modelled the impeller region as a turbulent swirling radial jet, although experimental measurements of the peak velocity and angle of the discharge flow are required to calculate the momentum source term. The accuracy of these approaches largely depends on empirical data which inevitably limits their range of applicability. Interface models, on the other hand, have been also used in the modelling of stirred tanks, using, for example, multiple frames of references (MFR) and sliding mesh (Kasat et al., 2008; Zadghaffari et al., 2009). In these approaches, the whole computational domain is divided into a stationary region, a rotating region surrounding the impeller and an interface in between. The sliding mesh approach is reported to be more accurate in predicting the turbulence properties of the flow than the MFR, but at a higher computational cost. The reason for this can be attributed to the transient nature of a sliding mesh simulation which requires a time-dependent flow field rather than allowing the use of a steady approximation and a time-averaged flow field as used in MFR (Singh et al., 2007). The interface model is capable of preserving the mesh quality but

requires momentum sources to account for the effect of moving grids. Additionally, numerical accuracy can be compromised due to the interpolation scheme used to balance mass and momentum across the interface. To date, most CFD studies have concerned an agitator with a prescribed motion, namely, the fluid flow has no influence on the motion of the agitator while the dynamics of the agitator in the ATR system is not predetermined as it is driven by both the fluid flow and collisions with the shaking tube. Therefore, accurate prediction of the flow field in the ATR system requires a CFD model capable of handling both structure-structure interaction (SSI), i.e. collision of the agitator with the tube and fluid-structure interaction.

Considerable efforts have been devoted to simulating fluid flows in the presence of immersed moving structures. One approach is to couple different numerical methods for the fluid flow and the motion of structures, for example, combining the finite element method (FEM) with CFD methods by meshing both fluid and solid phases. The flow field is first calculated using CFD methods by assuming the structure as a rigid boundary. The fluid force acting on the structure is then fed to the FEM to perform structural analysis (Cheng et al., 2005). The use of a single numerical method, such as FEM, has also been reported, for example the arbitrary Lagrangian-Eulerian (ALE) approach (Bathe et al., 1999) and deforming-spatial-domain/space-time methods (Tezduyar et al., 1992). The ALE-based FEM has been applied to study the migration (Villone et al., 2011) and alignment behaviours of particles in a viscoelastic fluid (Jaensson et al., 2016). It allows for large displacements and nonlinear material behaviour of the structure, but at a cost of low accuracy for highly deformable boundaries due to deterioration in the mesh quality (Udaykumar et al., 1996). On the other hand, Cartesian grid methods and the immersed boundary method (IBM) are based on an Eulerian formulation using a stationary mesh for the fluid. A solid then moves through the mesh according to a Lagrangian formulation (Balaras, 2004). The task of mesh generation is greatly simplified, and the mesh does not conform to the shape of the immersed structure. Solid structures are treated differently in the two approaches. In the former approach, the area covered by the solid structure is blanked out on a background Cartesian grid, resulting in fragmented control volumes (Quirk, 1994). Proper tracking schemes and interpolation methods are thus necessary to enforce boundary conditions in these cut cells (Quirk, 1994; Udaykumar et al., 1996). On the other hand, the IBM originally proposed by Peskin (1972) introduces a virtual

force field to match the fluid velocity with the motion of the solid structure (Fadlun et al., 2000). IBM is more efficient than the Cartesian grid method but it is also difficult to impose accurate boundary conditions, which can lead to inadequate representation of the boundary layer on the solid (Balaras, 2004).

The objective of this study is to establish numerical method for the ATR system as a first step towards understanding agitator's dynamics, fluid flow field and its mixing mechanism. In view of the key features of the ATR system, namely the co-existences of fluid-structure and structure-structure interactions, a new CFD model is proposed by combining the soft-sphere discrete element method (DEM) with a dynamic meshing approach referred as a coupled DEM-dynamic meshing (CDDM) model. To our knowledge, this is the first time that these two methods are combined to resolve the SSI and FSI simultaneously in the modelling of chemical reactors.

The accuracy of the CDDM model in handling the FSI problem is first verified against literature data on the sedimentation of a single sphere. The verified model is then applied to an ATR system agitated by a solid bar. The experimental measurement of fluid velocities in the ATR system is challenging due to the lateral shaking of the reactor body. Therefore, in this work, we do not attempt to carry out a detailed model validation for the ATR system due to the absence of appropriate data, but instead our aim is to understand the flow pattern and mixing mechanism under typical operational conditions. The performance of different pressure-strain models in the Reynolds stress model (RSM) employed to predict turbulent flow is also evaluated. Data analysis is focused on the dynamics of the agitator, its flow field and power consumption. The dominant mixing mechanism is elucidated by considering both the viscous and turbulent dissipations within the flow.

2. Computational model for multibody motion and fluid flow

2.1 Model development

In the present model, the solid body, or the structure, immersed in the fluid is regarded as a single element, as schematically shown in Fig. 2. By analogy with discrete element modelling, the structure's motion is tracked using Newton's second law of motion. Factors determining its motion are (i) gravity, (ii) hydrodynamic forces arising

from the fluid-structure interaction, and (iii) forces due to collision between solid bodies. The governing equation of the motion can now be written as:

$$\mathrm{m}\frac{d\mathbf{v}}{dt} = \mathbf{F}_f + \mathbf{F}_c + m\mathbf{g} \tag{1}$$

$$I\frac{d\boldsymbol{\omega}}{dt} = \mathbf{T}_f + \mathbf{T}_c \tag{2}$$

where m is the mass, I the moment of inertia, $\mathbf{v}$, $\boldsymbol{\omega}$, the translational and rotational velocities of the object, $\mathbf{F}_c$, $\mathbf{T}_c$ the force and torques due to collision between solid bodies, and $\mathbf{F}_f$, $\mathbf{T}_f$ the force and torques due to the hydrodynamic effect.

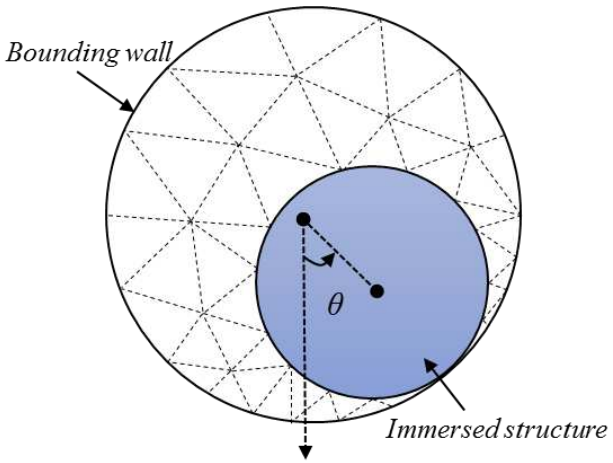

Fig. 2. Schematic demonstrating the modelling approach. θ defines the angular position of the immersed structure.

In terms of fluid forces, the present model simultaneously solves the multibody motion by modelling the collision using a soft-sphere model and resolving the fluid flow by solving the governing equations of the single-phase flow. In conventional CFD-DEM coupling, the fluid force imposed on the moving body is calculated by empirical or semi-empirical force laws. The cell size for CFD calculation is normally required to be larger than the size of the solid body. Consequently, the detailed flow structure, such as boundary layer, induced by the moving body cannot be resolved properly. In contrast, the present model calculates the fluid force by integrating the fluid stress $\boldsymbol{\sigma}$ over the surface of the movable body on a body-fitted tetrahedral mesh. The movement of the solid body is accommodated by dynamic meshing. The momentum change of the movable body inversely affects the flow field, achieving a two-way coupling between the fluid flow and multibody motion.

In terms of solid body forces, the collision between moving bodies is again modelled by a soft sphere model. It allows for overlap between solid bodies, thereby allowing the contact force to be determined. The collision force $\mathbf{F}_c$ includes the normal contact force $\mathbf{F}_{cn}$, the normal damping force $\mathbf{F}_{dn}$, the tangential contact force $\mathbf{F}_{ct}$ and the tangential damping force $\mathbf{F}_{dt}$, while the collision torque $\mathbf{T}_c$ is composed of $\mathbf{T}_t$ caused by tangential force and $\mathbf{T}_r$ due to rolling friction resulting from the elastic hysteresis losses or viscous dissipation (Zhou et al., 1999). The calculation of collision forces is based on the magnitude of overlap, in which the normal contact behaviour is described by Hertz theory while the tangential elastic frictional contact is based on Mindlin and Deresiewicz theory (Mindlin and Deresiewicz, 1953). Table 1 lists the equations used for the calculation of these forces. The details can be found elsewhere (He et al., 2018a; He et al., 2015; He et al., 2018b).

Table 1 Equations used to calculate forces and torques in this work.

Terms	Equation
Fluid force	$\mathbf{F}_f = \oiint \boldsymbol{\sigma} \cdot \hat{\mathbf{n}}\, dS$
Fluid torque	$\mathbf{T}_f = \oiint \mathbf{R} \times (\boldsymbol{\sigma} \cdot \hat{\mathbf{n}})\, dS$
Normal contact force	$\mathbf{F}_{cn} = \frac{4}{3} E^* R^{*1/2} \delta_n^{3/2} \hat{\mathbf{n}}$
Normal damping force	$\mathbf{F}_{dn} = c_n \left(8 m^* E^* \sqrt{R^* \delta_n}\right)^{1/2} \mathbf{v}_n$
Tangential contact force	$\mathbf{F}_{ct} = -\mu_t \lvert \mathbf{F}_{cn} \rvert \left[1 - \left(1 - \frac{\min(\lvert \boldsymbol{\delta}_t \rvert, \delta_{t,\max})}{\delta_{t,\max}} \right)^{3/2} \right] \hat{\boldsymbol{\delta}}_t$
Tangential damping force	$\mathbf{F}_{dt} = -c_t \left(6 \mu_t m E^* \lvert \mathbf{F}_n \rvert \frac{\sqrt{1 - \lvert \boldsymbol{\delta}_t \rvert / \delta_{t,\max}}}{\delta_{t,\max}} \right)^{1/2} \mathbf{v}_t$
Torque due to tangential force	$\mathbf{T}_t = (\mathbf{F}_{ct} + \mathbf{F}_{dt}) \times \mathbf{R}$
Rolling torque	$\mathbf{T}_r = \mu_r R \lvert \mathbf{F}_{cn} \rvert \hat{\boldsymbol{\omega}}_n$

In Table 1, the effect radius R^* is calculated as,

$$1/R^* = 1/R_i + 1/R_j \tag{3}$$

with R_i and R_j being the radius of two bodies in contact. The effect elastic modulus E^* is calculated as,

$$\frac{1}{E^*} = \frac{(1-\nu_i^2)}{Y_i} + \frac{\left(1-\nu_j^2\right)}{Y_j} \tag{4}$$

where Y_i and ν_i are the Young's Modulus and Poisson's ratio of particle i, respectively; δ_n and $\boldsymbol{\delta}_t$ represent the overlap in normal and tangential directions;

$$\delta_{t,\max} = \frac{\mu_t(2-\nu)\delta_n}{2-2\nu} \tag{5}$$

with μ_t the sliding friction and μ_r the rolling friction and $\widehat{\boldsymbol{\delta}}_t = \boldsymbol{\delta}_t/|\boldsymbol{\delta}_t|$.;

$$\widehat{\boldsymbol{\omega}}_n = \boldsymbol{\omega}_n/|\boldsymbol{\omega}_n| \tag{6}$$

with $\boldsymbol{\omega}_n$ the angular velocity; The damping coefficient can be linked to the restitution coefficient e as,

$$c_n = \frac{\ln(e)}{\sqrt{\pi^2 + \ln^2(e)}} \tag{7}$$

where e is defined as the ratio of post-collisional contact velocity to the pre-collisional contact velocity and c_t is the tangential damping coefficient.

2.2 Model implementation

The commercial CFD software, ANSYS Fluent v17.1, was used as the modelling platform to solve the standard continuity and Navier-Stokes equations, closed using the turbulence models discussed further below, based on a finite-volume discretization scheme.

For dynamic meshing, there are three types of meshing methods available in ANSYS Fluent, namely, smoothing, dynamic layering and remeshing. Mesh smoothing only works on interior cells by adjusting the position of nodes to improve cell quality, without affecting the number of nodes and their connectivity. Dynamic layering is only applicable to prismatic meshes by adding or removing layers of prismatic cells adjacent to a moving boundary to account for its translational motion. It is thus not applicable for the multibody motion discussed here. Remeshing, on the other hand, agglomerates degenerated cells and then locally remeshes those agglomerated cells or faces. In the present study, the smoothing and remeshing methods were adopted for dynamic meshing. For spatial discretization, an inflation layer of prismatic cells was created on the surface of the solid body while the rest of the domain was discretized using tetrahedral cells due to its compatibility with remeshing. The inflation layer was grouped into a separate cell zone. By doing so, rigid body motion was also specified

to the inflation layer to preserve the cells throughout the simulation and the remeshing/smoothing is only performed on the remaining tetrahedral CFD cells. Remeshing is triggered only when the size and skewness (defined as the difference between the shape of the cell and the shape of an equilateral cell of equivalent volume) of the cell exceeds a specified threshold. It is worth noting that the current approach requires a finite space between the surfaces of two approaching bodies due to the use of attached rigid prism layers. This is resolved by using a virtual collision radius that is slightly larger than the actual body radius to avoid mesh deformation of the boundary layer. This virtual collision radius is then determined by the physical size of the solid body and also the thickness of the inflation layer. In some cases, if resolving the boundary layer is not a critical issue, the virtual collision radius can be the same as that of the physical collision radius. However, it has no effect on the ATR system discussed above since direct physical contact between the agitator and the tube is avoided through the use of end caps attached to the ends of the agitator, hence leaving a gap between the internal agitator and the external tube. Therefore, the virtual collision radius for ATR system is the same as the size of the plastic cap.The proposed model was fully implemented through the user defined functions. Based on this general purpose fluid flow solver, there is no limitation to the complexity of the geometrical structure of the immersed solid body, whereby the incorporation of new designs of immersed structure is readily accomplished.

The calculation sequence was as follows. At each CFD time-step, the hydrodynamic forces and torques acting on the immersed body were evaluated by summing up (discrete integration) the pressure and viscous stress over its surface after resolving the surrounding flow field. The collision forces were calculated only if the solid body was in contact with the bounding walls. The translational and angular velocities of the solid body were then calculated from the resulting forces and torques by means of an explicit time integration method (forward Euler method), which were later assigned to the immersed object as a boundary condition in the CFD solver. The CFD solver subsequently used this information data to determine the new position of the object and to update the flow field for the next time-step. It is worthwhile to note that CFD time step is not only limited by the CFL(Courant-Friedrichs-Lewy) condition but also the propagation of Rayleigh wave between two colliding bodies, as it needs to be sufficiently small to resolve the collision between solid bodies (Zhu et al., 2007).

3. Validation of fluid structure interaction: falling sphere

To validate the proposed CDDM model, the settling of a single sphere in silicon oil was simulated, for which detailed experimental measurements of trajectories and velocities of the sphere are available (ten Cate et al., 2002). This test serves as a validation of the proposed method in handling FSI problems and is closely related to the modelling of the ATR system since the fluid force plays a key role in determining the displacement and the flow field surrounding the free-moving object in both cases. A schematic view of the simulation setup is shown in Fig. 3. A spherical particle with a diameter of 15 mm and density of 1120 kg m^{-3} was released from a height of 120 mm in a closed box. Different combinations of viscosity and density were considered in the experimental work of (ten Cate et al., 2002), resulting in four Reynolds numbers, Re, as listed in Table 2, where the Re is defined based on the terminal velocity of a sphere in an infinite medium (ten Cate et al. (2002). The relation for the drag coefficient C_{d} due to (Abraham, 1970) was used to determine the terminal velocity U_{∞}, given as:

$$C_{\mathrm{d}} = \frac{24}{(9.06)^2}\left(\frac{9.06}{\sqrt{Re}} + 1\right)^2 \tag{8}$$

with the characteristic time t_{∞} defined when the velocity of the sphere reached 99.99% of the terminal velocity. As shown in Table 2, the difference between predicted (U_{sim}) and theoretical (U_{∞}) terminal velocities is within 10%, with the difference mainly due to wall effects, while the average difference with experimental (U_{exp}) values is less than 5%.

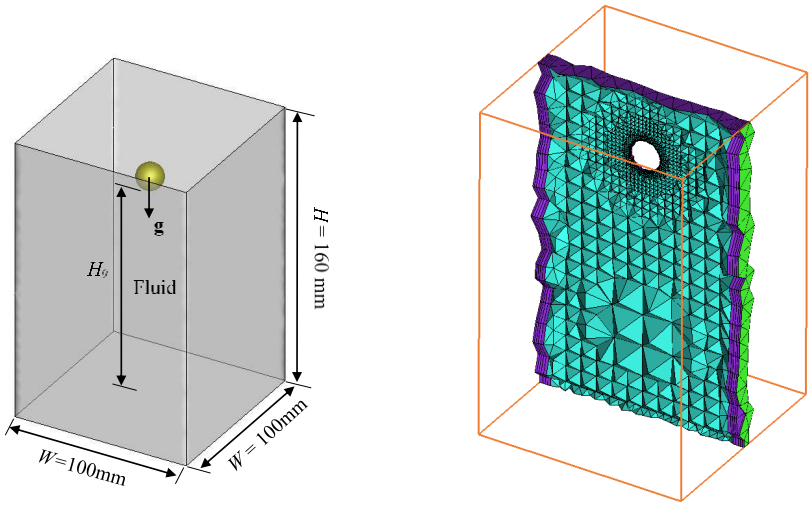

(a) (b)

Fig. 3 (a) Schematic view and (b) mesh representation of the simulation of a single settling sphere (only the central slice is shown).

Table 2 Experimental conditions, and measured and predicted terminal velocities.

Case	Fluid		Re	t_∞(s)	Terminal velocity (m s^{-1})			$\frac{U_{\mathrm{sim}}}{U_\infty}$	$\frac{U_{\mathrm{sim}}}{U_{\mathrm{exp}}}$
	Density (kg m^{-3})	Viscosity (Nsm^{-3})			U_∞	U_{exp}	U_{sim} (Standard deviation)		
1	970	0.373	1.50	0.182	0.038	0.0369	0.0349 (4.9×10^{-5})	0.918	0.946
2	965	0.212	4.10	0.263	0.060	0.0589	0.0576 (3.5×10^{-4})	0.960	0.978
3	962	0.113	11.6	0.366	0.091	0.0871	0.0875 (7.5×10^{-5})	0.962	1.004
4	960	0.058	31.9	0.476	0.128	0.1232	0.1220 (2.8×10^{-4})	0.953	0.990

Fig. 4 compares the sphere trajectories and settling velocities obtained experimentally and using the present model for the four cases listed in Table 2. The variation of the transient velocity of the sphere suggests that it experiences three stages during settling: a short period of acceleration, steady fall and a quick deceleration when approaching the bottom wall. As shown in Fig. 4, the predicted trajectories and velocities of the falling sphere are in good agreement with the experimental measurements. The dynamic motion of the sphere in the high Re case, case 4, is well captured. Some discrepancy is, however, noticeable for the case of the smallest Reynolds number (case 1) when the sphere is close to the bottom of the box. This implies that the model is weakly sensitive to the Reynolds number. The discrepancies observed in the acceleration period may be due to experimental error, such as release of the sphere in experiments, and numerical error due to interpolation of the velocity from the trajectory of the sphere and resolution of high speed camera. Discrepancies in the near wall region can be to some extent attributed to the presence of the attached rigid prismatic cells of the boundary layer which prevents the sphere from contacting with the bottom wall. This is also the reason why the height of the sphere does not reduce to zero, as shown in Fig. 4(b). For the ATR system, however, there are caps at both ends of the agitator to prevent direct contact with the external tube. It is thus reasonable to assume that the present model is adequate for the simulation of the ATR system.

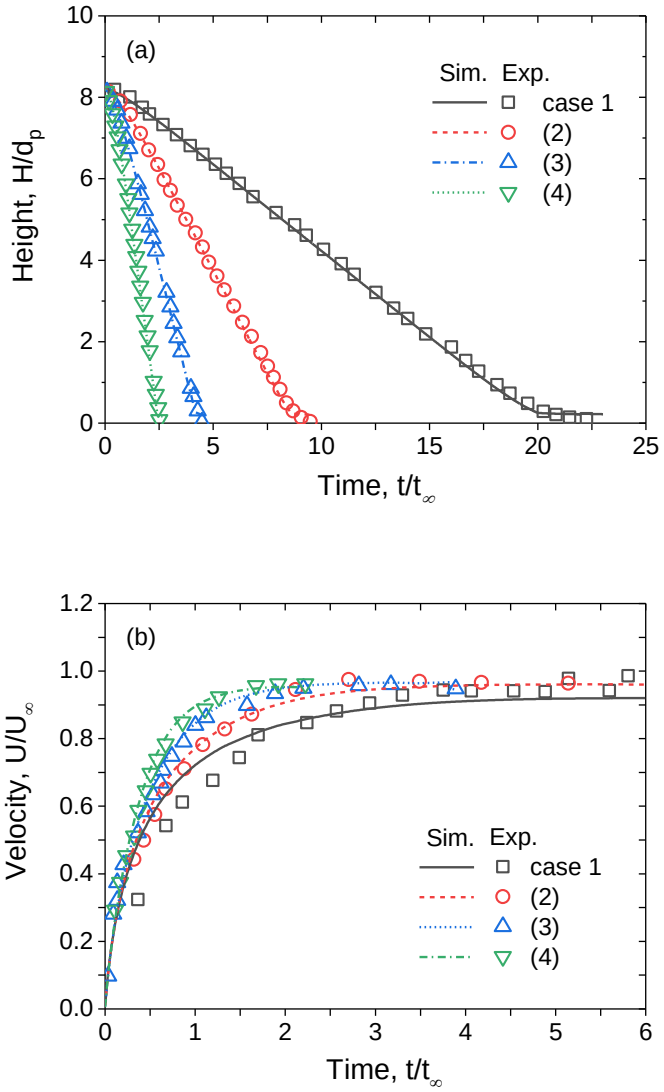

Fig. 4. Comparison between (a) trajectories and (b) velocities of a falling sphere obtained by simulation and measurement (ten Cate et al. (2002).

Apart from sphere motion, the prediction of the flow field is equally important. Fig. 5 shows the predicted flow fields for two cases: Re = 1.5 and Re = 31.9. For the larger Re, the wake behind the failing sphere is more developed and elongated. When the sphere approaches the bottom of the box, both cases show a deformed flow in front of the sphere, leading to a lateral motion of the fluid. The profiles of vertical velocity noted above are qualitatively in line with those obtained using the lattice-Boltzmann method (ten Cate et al., 2002). According to ten Cate et al. (2002), the difference in the shape of the flow field is related to the ratio of the particle advection time ($\tau_a \approx d_p/u_\infty$) and the momentum diffusion time ($\tau_\nu \approx d_p^2/\nu$) at different Reynolds numbers.

For large Re, the momentum takes longer time to diffuse than particle advection, thereby leading to an elongated wake.

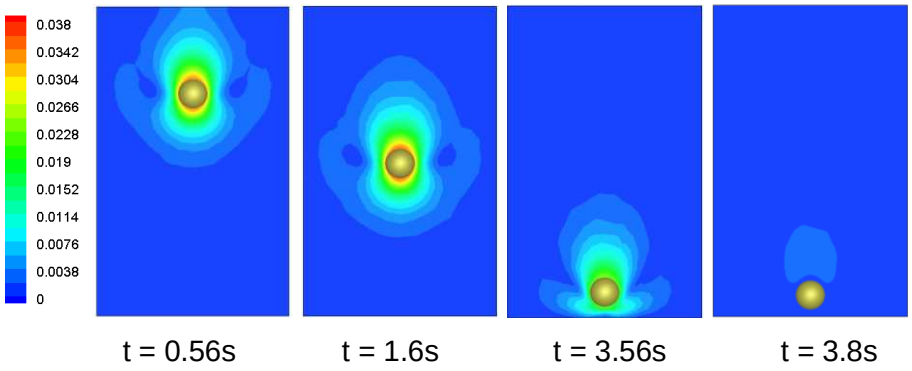

(a)

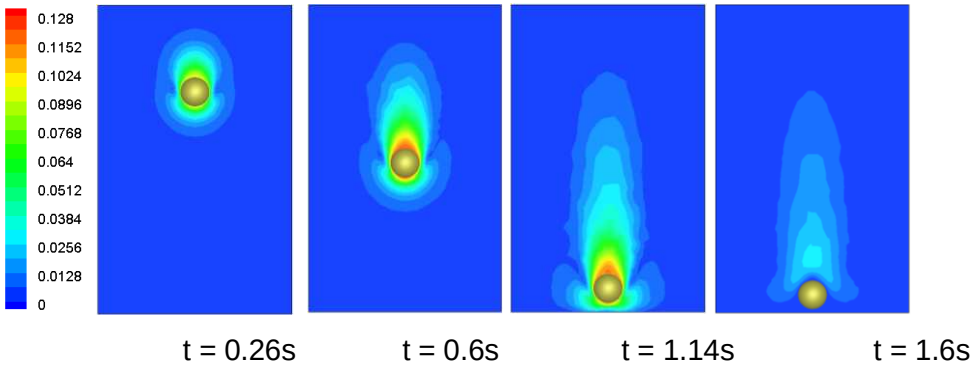

(b)

Fig. 5 Contours of velocity magnitude during a sphere settling at (a) Re = 1.5 and (b) Re = 31.9.

In terms of energy dissipation, the faster the sphere moves, the more energy is imparted to the fluid and thus a larger volume is required to convert this to heat. Since the Reynolds number of sedimentation is quite low (Re < 32), the majority of the energy is consumed through viscous dissipation. Hence, the total energy dissipation rate can be estimated by integrating the viscous dissipation over the whole volume of the fluid, which can be given as,

$$\varepsilon = \int \boldsymbol{\tau}\dot{\boldsymbol{\gamma}} dV \tag{9}$$

with $\boldsymbol{\tau}$ being the fluid stress and $\dot{\boldsymbol{\gamma}}$ the strain rate. After the sphere reaches the terminal velocity, the rate of energy input is due to the loss of potential energy which can be calculated as,

$$\left(\rho_{\mathrm{p}} - \rho_{\mathrm{f}}\right) g V_{\mathrm{p}} U_{\max} \tag{10}$$

where V_p is the volume of the sphere and U_{max} is the terminal velocity the sphere reaches without the influence of the bounding walls. As shown in Fig. 6, the rate of energy consumption due to viscous dissipation at the terminal velocity matches well with the rate of energy input due to the loss of potential energy, with differences of within 5% further confirming the validity of the present model in predicting fluid-structure interaction from the perspective of energy conservation.

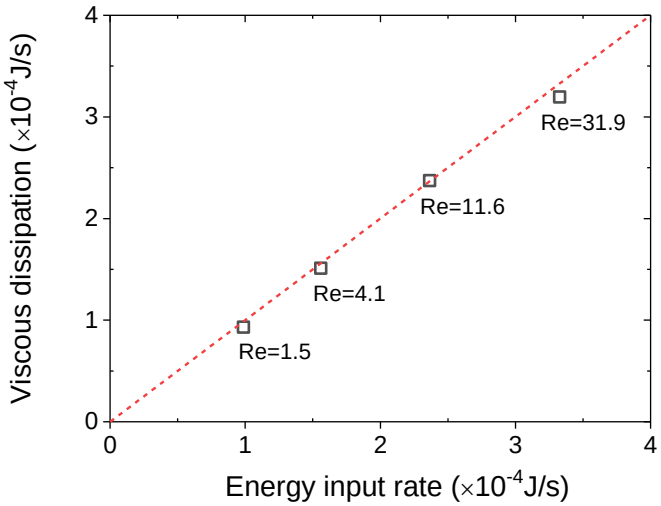

Fig. 6 Comparison of energy input and consumption rate due to viscous dissipation.

4. Application to ATR system agitated by a solid bar

4.1 ATR model setup and simulation conditions

Basic hydrodynamic parameters, such as the characteristic velocity or a Re number, are generally not available for the ATR systems. However, the system has two directions of motion, a horizontal motion driven by the lateral oscillation, and a pressure driven axial flow. The axial flow velocity can be used to define an axial Reynolds number:

$$Re_{ax} = \frac{\rho D_t V_{ax}}{\mu} \tag{11}$$

with D_t the diameter of the reactor tube. The temporal velocity and displacement of the lateral oscillation were modelled as sinusoidal motion, given by:

$$U(t) = 2\pi f A\cos(2\pi f t) \tag{12}$$

$$X(t) = A\sin(2\pi f t) \tag{13}$$

with f the excitation frequency and A the oscillation amplitude. The lateral oscillation was imposed as a velocity boundary condition in the CFD code. Radial mixing is driven

by the agitator. As the agitator speed relative to the external wall is unknown, we define a characteristic radial velocity $V_{\max}$ based on the maximum speed of lateral oscillation, which is calculated as:

$$V_{\max} = 2\pi f A \tag{14}$$

The agitator, or radial, Re_{r} can now be defined based on the maximum lateral speed, and the agitator diameter D_{a}:

$$Re_{\mathrm{r}} = \frac{\rho D_{\mathrm{a}} V_{\max}}{\mu} \tag{15}$$

In the present study, an ATR system agitated by a solid bar is investigated. The diameter of the agitator and the external tube are 14 mm and 22 mm, respectively, as shown in Fig. 7(a). The device is designed for residence times of 2-60 min resulting in a superficial axial velocity V_{ax} between 0.00123 m s^{-1} and 0.0368 m s^{-1}. The corresponding Re_{ax} ranges from 27 to 810. Typically, the lateral motion is the result of frequencies f between 1 and 6 Hz and amplitudes A of 10-25 mm, giving a radial Re_{r} between 800 and 13,000. Comparing the radial and axial Reynolds numbers it is clear that the motion in the device is dominated by radial flows induced by the lateral movement.

It is prohibitive to model the whole length of the reactor tube mainly due to the computational expense associated with dynamic meshing and turbulence modelling. Hence, only a section of the ATR system with a length of 44 mm was modelled. A periodic boundary condition was applied in the axial direction by imposing a mean pressure gradient as a source term to the momentum equations used to derive the axial flow. The working fluid was water. For the periodic condition, a mass flow rate of 0.002 kg s^{-1} was imposed along the axial direction of the reactor tube which corresponds to a superficial axial velocity of 0.0088 m s^{-1}. In the simulations, a constant frequency of 5 Hz and amplitude of 12mm were used (see Table 3). For the simulated case, the axial Reynolds number Re_{ax} was 192 based on the axial flow rate while the radial Reynolds number Re_{r} was 5268 based on the maximum velocity of the tube. Fig. 7(b) shows the initial computational mesh used in this study, which consists of two components: a prism mesh in the boundary layer and a tetrahedral mesh in the rest of the computational domain. An enhanced wall treatment was used with the turbulence modelling in the near-wall boundary layer to capture the flow characteristics in the viscous sub-layer.

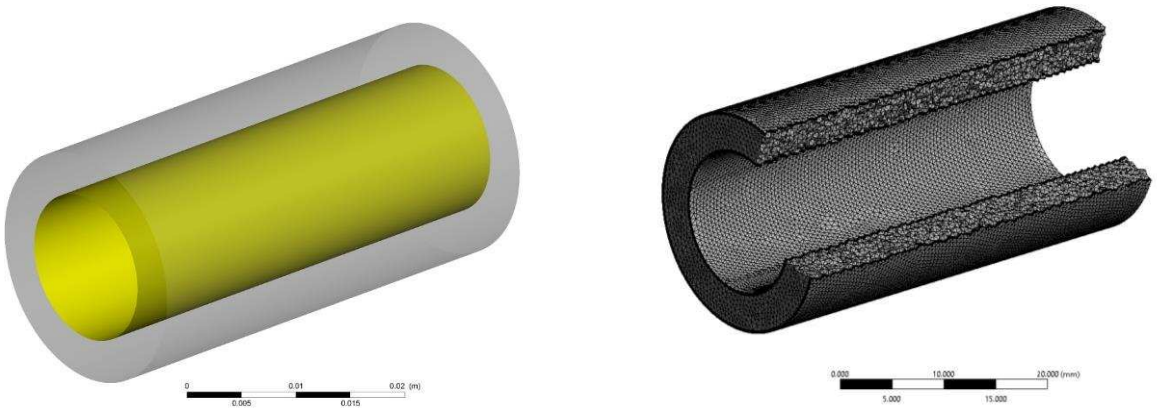

(a) (b)

Fig. 7. (a) Geometrical and (b) mesh representation (cut by two planes for better visualization) of the simulated ATR system agitated by a solid bar (caps are not shown).

As shown in Fig. 1, end caps are present to prevent the agitator from direct contact with the reactor tube. To model structure-structure interaction, the collision diameter used to determine when a collision between the agitator and the reactor tube happens was thus determined by the size of the end caps. All the parameters used in the simulations are summarized in Table 3, which are typical of design and operational parameters. Initial sensitivity studies showed that the contact parameters, such as the Young's modulus, Poisson ratio, sliding friction and damping coefficients, have little impact on the dynamics of the internal agitator. The rolling friction coefficient affects the rotational speed of the agitator, whose value was chosen to give a typical peak rotational speed around 10 rad/s.

Table 3 Parameters used in simulations.

Parameters	Value
Amplitude, A (mm)	12
Frequency, f (Hz)	5
Thickness of end cap, S_{cap}(mm)	1.0
Mass of agitator, m (kg)	0.0846
Moment of Inertia, I (kg m^2)	7.191×10^{-6}
Young's modulus, E (Pa)	1.0×10^{8}
Poisson ratio, *v*	0.3

Rolling fiction coefficient, μ_{r}	0.02
Sliding friction coefficient, μ_{t}	0.3
Damping coefficient, $c_{\mathrm{n}}, c_{\mathrm{t}}$	0.2
Fluid density, ρ (kg m^{-3})	998.2
Viscosity, μ (kg m^{-1} s^{-1})	0.001

Sub-processes, such as bubble collision, and particle dispersion, depositions and resuspension that may occur in certain types of ATR require accurate prediction of the turbulence in the reactor. Power consumption is also often used as a criteria for device scaling, and this also calls for accurate predictions of turbulence levels. In this study, turbulence in the ATR system was modelled using a Reynolds stress model (RSM). The RSM explicitly solves transport equations for each component of the Reynolds stresses without relying on the hypothesis of an isotropic eddy-viscosity. The stress equations are solved in conjunction with an equation for the turbulence energy dissipation rate. The effect of the anisotropic nature of turbulence is accounted for in Reynolds stress models in a more rigorous manner. It is thus expected to yield more accurate predictions of the flow in the ATR system. In the RSM, the stress transport equation is written as:

$$\frac{\partial}{\partial t}\left(\rho\overline{u_i'u_j'}\right) + \frac{\partial}{\partial x_k}\left(\rho u_k\overline{u_i'u_j'}\right) = D_{T,ij} + D_{L,ij} + P_{ij} + \Pi_{ij} + \varepsilon_{ij} + S \qquad (16)$$

with the two terms on the left hand side being the local time derivatives of the stress and convective transport, respectively, $D_{T,ij}$ is the turbulent diffusion term, $D_{L,ij}$ the molecular diffusion term, P_{ij} the stress production term, Π_{ij} the pressure-strain term, ε_{ij} the dissipation term and S a source term. The pressure-strain term acts to redistribute energy among Reynolds stresses. Thus, the performance of an RSM strongly depends on the closure model for the pressure-strain correlation.

In this study, the performance of three models for the pressure-strain term was evaluated, namely the quadratic pressure-strain model (Speziale et al., 1991), the stress-omega pressure-strain model (Wilcox, 1998) and the stress-baseline (BSL) pressure-strain model. The quadratic model is based on an ε-equation (where ε is the turbulence energy dissipation rate) and uses a quadratic relation for the pressure-strain correlation, while the other two models are ω-based ($\omega = \varepsilon/k$, with ω the

specific dissipation rate and k the turbulence kinetic energy) and use a linear model for the pressure-strain correlation. The advantage of the ω-based equations is that they allow for a more accurate near-wall treatment by automatically switching from a wall function to a low-Reynolds number formulation based on the mesh spacing. Compared to the stress-omega pressure strain model, the stress-BSL pressure-strain approach adopts a blending between the k-ω model near the surface and the k-ε model in outer regions of the flow, and thus removing the sensitivity to freestream conditions observed with the stress-omega pressure-strain model.

For discretization, the least squares cell-based gradient method was adopted, whilst the QUICK scheme was used for momentum and a second-order scheme for pressure interpolation. The SIMPLE scheme was used for pressure-velocity coupling. The method is second-order accurate in both time and space.

4.2 Grid independence

Grid resolution is a key factor affecting the numerical accuracy and the computational expense of CFD simulation. Common practice is to perform sensitivity tests to grid resolution by refining the finite-volume cell size and/or its distribution until no noticeable difference is observed in the flow variables of interest. However, the cell number cannot be maintained during the process of remeshing due to the continuously deforming domain. In fact, the cell number during remeshing is indirectly controlled by the thresholds of the cell size and the cell skewness, beyond which the cells are marked for smoothing or remeshing at the next time step.

In this study, variation in grid resolution was achieved by starting from the same initial grid while using different criteria for remeshing. The threshold of cell skewness was set to 0.75 to avoid excessive deformation of the grid cell. Variation in grid resolution was accomplished by using different size thresholds: 0.8mm, 1.0mm and 1.2mm. For this exercise, turbulence was modelled using RSM with the quadratic pressure-strain model. By tracking the cell number in the system, significant fluctuations in that number were observed during the process of remeshing, as shown in Fig. 8. This is primarily caused by the periodic motion of the agitator, leading to a repeatable change of the computational domain. The number of the grid cells increases with decreasing

threshold of the cell size. The degree of fluctuation in the cell number for the smallest size threshold (0.8mm) is lower than for the other cases, suggesting that grid resolution can be better preserved by a smaller size threshold during the process of remeshing.

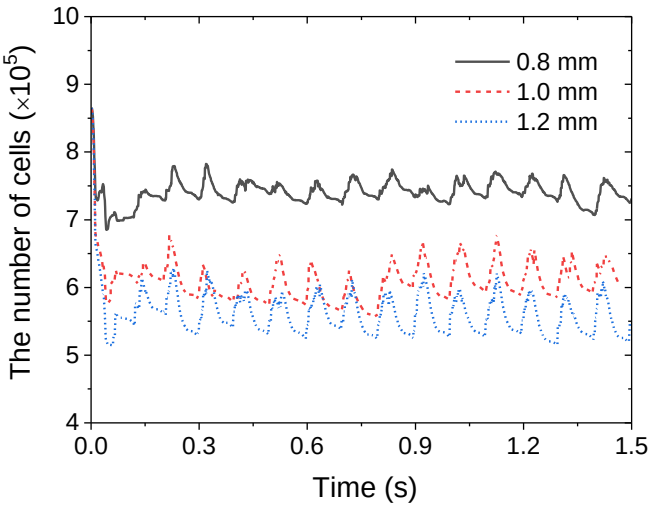

Fig. 8. Time evolution of the number of grid cells of the simulated ATR system.

Fig. 9 shows the temporal evolution of the relative translational and angular velocities of the agitator. Regular fluctuating patterns are observed shortly after the start-up phase, indicating a well-behaved periodicity. The results from the different size thresholds collapse onto each other, with a standard deviation smaller than 0.01%. This therefore suggests that the effect of grid resolution on the motion of the agitator is very small within the considered size range.

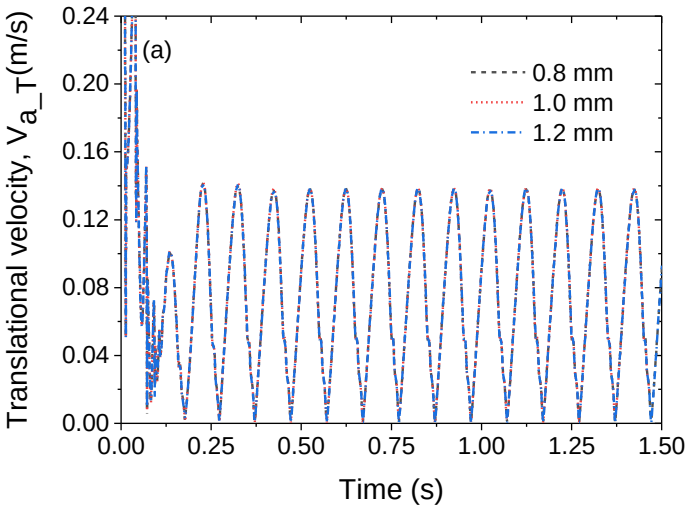

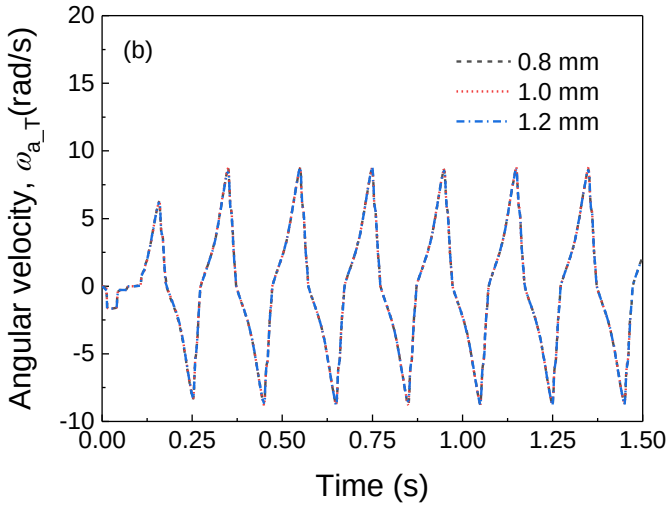

Fig. 9. Influence of size threshold of dynamic meshing on the motion of the agitator in the reference frame of the tube: (a) translational motion and (b) rotational motion.

The same conclusion can also be drawn regarding the induced flow structure. Fig. 10 shows the mean velocity profile of the fluid along a vertical line located at the centre of the reactor tube. The velocities are sampled in the reference frame of the tube. There is no velocity information in the range of -6 mm to 4 mm due to the presence of the agitated bar. Three different phases are selected, with no notable difference observed. Similar results were found to for the fluid's turbulence quantities. Since both the agitator's motion and the induced flow structure show negligible variation, it is reasonable to conclude that the selected grids are well suited for the flow analysis in the ATR system. Nevertheless, to be conservative, the analysis that follows is based on the case with a size threshold of 0.8 mm during dynamic meshing.

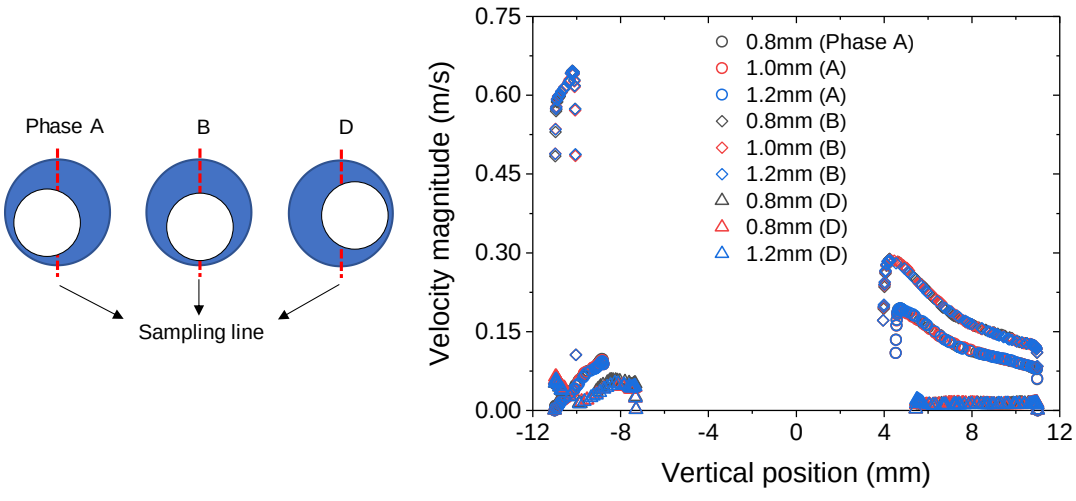

Fig. 10. Profile of fluid mean velocity along the vertical middle line obtained using different size thresholds of dynamic meshing at different phases, in which phase A = 0, B = 0.2π and D = 0.7π.

4.3 Dynamics of the agitator

Due to the periodicity of the sinusoidal shaking, phase-averaged results are presented in the following. A total physical time of 4 s was simulated, corresponding to 20 periods of oscillation. Simulation was sampled after an initial period of 2 s. The choice of pressure-strain term in the RSM was found to have a negligible impact on the motion of the agitator, hence only the results derived using the quadratic pressure-strain model are shown below. The displacement of the reactor tube and the agitator, shown in Fig. 11(a), and the velocity of the tube, Fig. 11(b), are presented in the global reference frame; while the velocity of the agitator is presented in the reference frame of the tube, Fig. 11(b). This is done as it is the relative velocity that is driving the flow inside the tube.

The maximum relative velocity of the agitator is approximately 0.138 m/s which is about 36.6% of the maximum velocity of the shaking tube. If the radial Reynolds number were redefined based on the agitator's velocity, Re_{r} would change from 5268 to 1928, indicating a transitional flow regime. Overall, the motion of the agitator shows a phase lag compared that of the tube. From phase 0 to π/2, the reactor tube moves toward the right hand side with a decreasing velocity, while the agitator accelerates towards the bottom of the tube followed by a deceleration when it moves upwards. During this stage, the angular velocity of the agitator increases from 2.25 rad/s to a peak of 8.81 rad/s at phase 0.5π (Fig. 11(c)), suggesting that the frictional force resists translational motion whilst it facilitates rotation. After 0.5π, there is a small fluctuation in the agitator's velocity, especially in the vertical direction. This is mainly caused by the reverse of the tube's direction of motion which increases the contact force and thus the frictional force acting on the agitator. In addition, the reduction in the angular velocity of the agitator indicates that friction starts to facilitate translational motion, resulting into a slight increase in the translational velocity (Fig. 11(b)). Fig. 11(d) shows the overlap δ used in the calculation of contact force between the agitator and the tube, where $\delta = d + r + S_{\mathrm{cap}} - R$, with d the distance between the agitator's centre and the

centre of the moving tube, r is the radius of the agitator and R the radius of the tube. The variation of the overlap is less than 4% of the end cap's thickness and always greater than 0, indicating that the agitator does not bounce off the surface of the tube during oscillation. Fig. 11(e) plots the velocity magnitude as a function of the angular position of the agitator, where the angular position is defined based on the centre of the oscillating tube, as indicated in Fig. 2. It is found that the moving regime of the agitator is between -72º and 72º. The agitator follows different velocity paths when it moves up and down. Moreover, the location of the maximum velocity does not occur at the bottom of the tube (θ=0º). The maximum velocity occurring at a negative angle is mainly due to the phase lag between the motion of the agitator and the oscillation of the external tube. As shown in Fig. 11a, when the agitator reaches the bottom of the tube (0.2π), the external tube is still accelerating and thus leading to further increase of agitator's velocity.

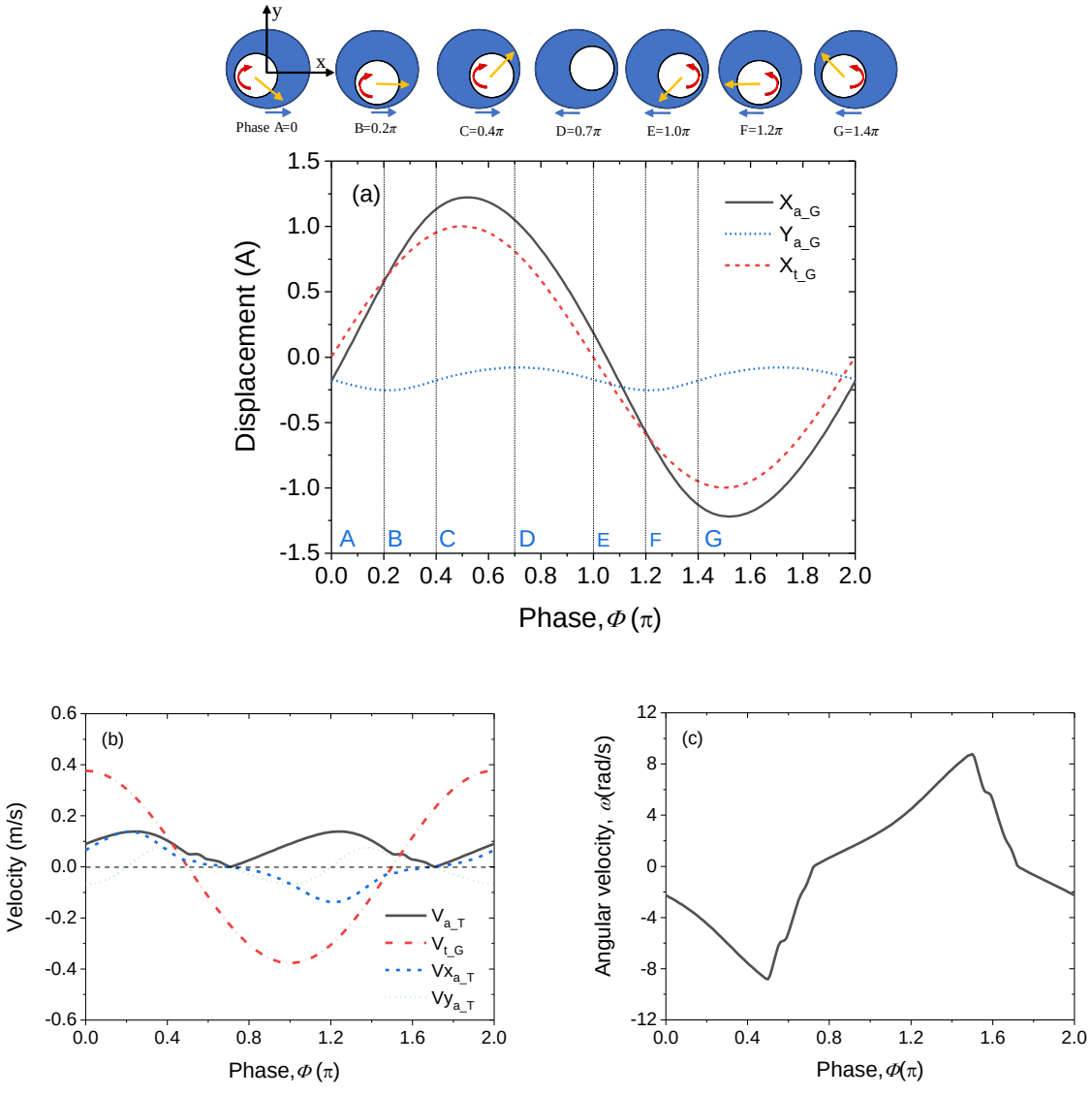

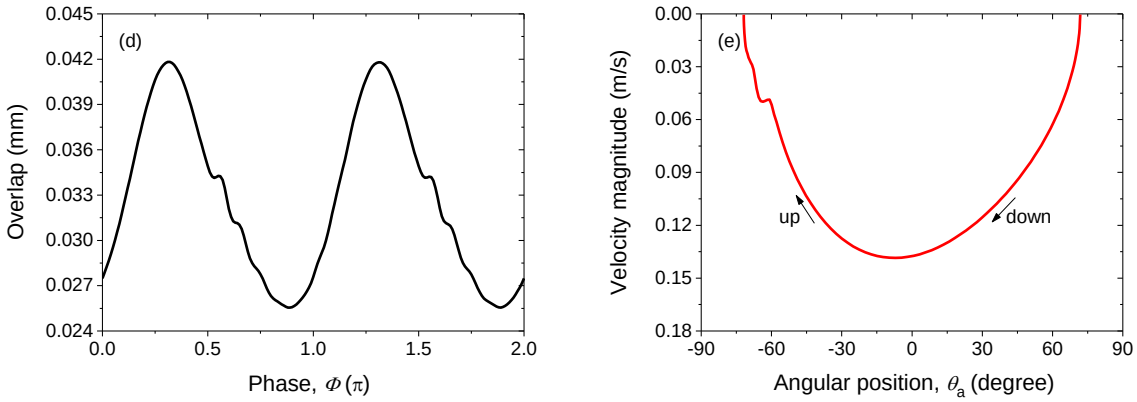

Fig. 11. (a) Displacement of the agitator (X_{a_G}, Y_{a_G}) and the tube (X_{t_G}) in the global reference frame, nondimensionalized by the amplitude of shaking and illustration of seven selected phases: A=0, B=0.2π, C=0.4π, D=0.7π, E=1.0π, F=1.2π and G=1.4π., (b) translational velocity of the agitator in the reference frame of the tube (V_{a_T}, Vx_{a_T} and Vy_{a_T}) and translational velocity of the tube (V_{t_G}) in the global reference frame, (c) angular velocity of the agitator (ω_a), (d) overlap during collision force calculation, and (e) Velocity of the agitator as a function of angular position in the reference frame of the tube, where θ_a is defined relative to the vertical line at the centre of the tube, as shown in Fig. 2.

In the ATR system, the agitator is driven by a combination of gravitational, fluid and contact forces due to interaction with the reactor tube. The present model allows for a direct comparison of these forces due to their explicit consideration in the collision model. Fig. 12 shows the pressure and viscous force due to fluid flow predicted by different pressure-strain models in the RSM during an oscillation period. The trends of these two forces are similar for different pressure-strain models. During the period of upward agitator motion ($0.2\pi<\Phi<0.7\pi$), there is a sudden increase in the pressure following a sharp drop, which is related to the slight increase of the translational velocity due to the reverse of the tube oscillation. This slight increase of the translational velocity likely also leads to the increase of the viscous force. However, this effect is offset by the decreasing angular velocity, thus leading to a continuous reduction in the viscous force. At the stage of downward motion ($0.7\pi<\Phi<1.2\pi$), both the pressure and the viscous force show a considerable increase due to the combined effect of the increasing translational and rotational velocities. Comparable results were also obtained by the other pressure-strain models. The pressure predicted by the

quadratic model is in general slightly lower than that of the other pressure-strain models, while the vicious force predicted by the quadratic model is significantly smaller. It should be noted that the magnitude of fluid forces are much smaller compared to that of the collision force, suggesting that the motion of the agitator is mainly dominated by inertia and interaction with the tube and thus the dynamics of the internal agitator is somewhat independent on the choice of turbulence model.

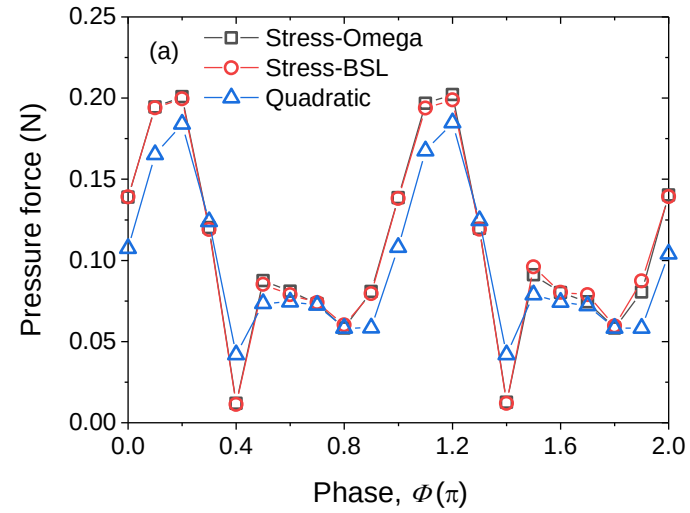

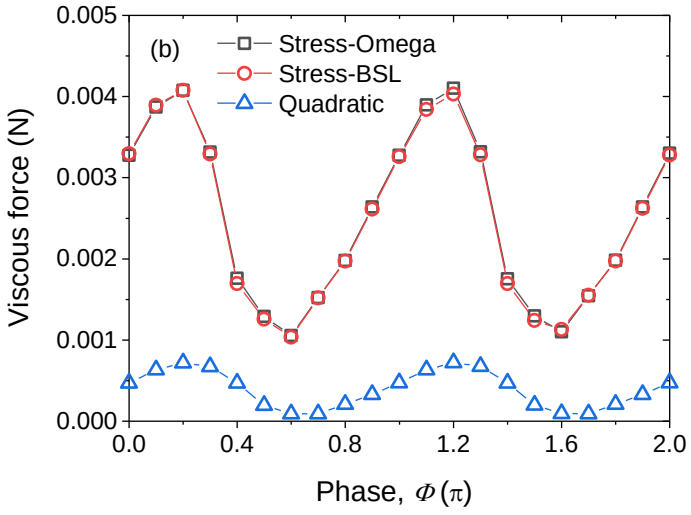

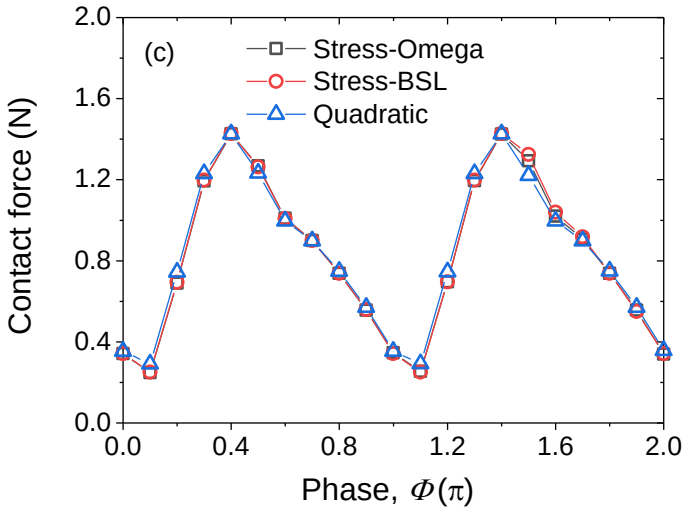

Fig. 12. Comparison of (a) pressure force, (b) viscous force and (c) contact force acting on the agitator by different pressure-strain models in the RSM.

4.4 Induced flow structure

To better assess the performance of the different pressure-strain models in the RSM, comparisons are made in terms of both the flow pattern and turbulence quantities at different phases (seven in total), as illustrated in Fig. 13(a). The results of a laminar flow model are also presented for comparison. An illustration of the agitator's position together with its rotational direction are also shown in Fig. 13. The agitator in phases C, E and G is located at the same vertical position as in phase A, but with a different direction of motion. The agitator in phases B and F is located at the bottom of the tube, while the agitator reaches its highest point during the oscillation in phase D.

Fig. 13 shows the velocity profile of the fluid flow in the reference frame of the tube. The velocity distributions are comparable amongst all the models, with large values localized in the contact region between the agitator and the reactor tube. The fluid is squeezed out of the contact region, forming a local region with low pressure. Similar magnitude of the fluid velocities are obtained by the stress-omega and stress-BSL pressure-strain models, which are close to that of the laminar model but slightly larger than that of the quadratic model. The difference is more significant when the agitator reaches the highest point (in phase D). Moreover, the velocity distribution of the quadratic pressure-strain model is smoother than that of the other two approaches, indicating larger dissipation by turbulence. This is primarily related to the fact that both

the stress-omega and the stress-BSL pressure-strain models are based on turbulence frequency, whilst quadratic model is based on turbulence eddy dissipation.

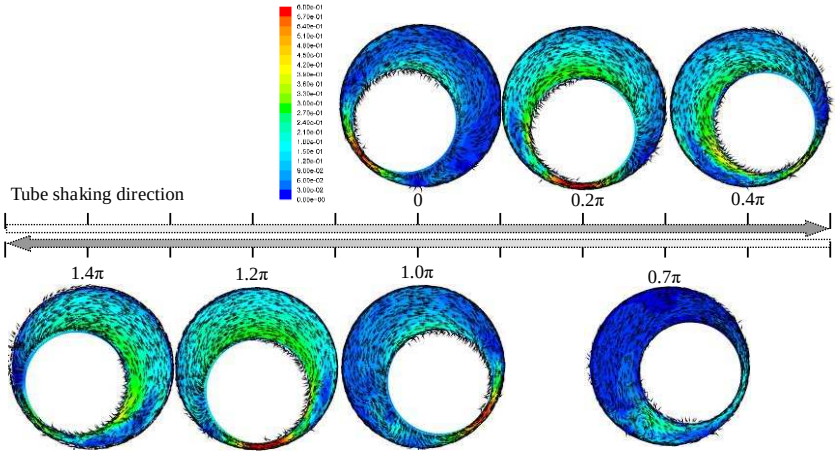

(a) Stress-omega pressure-strain model

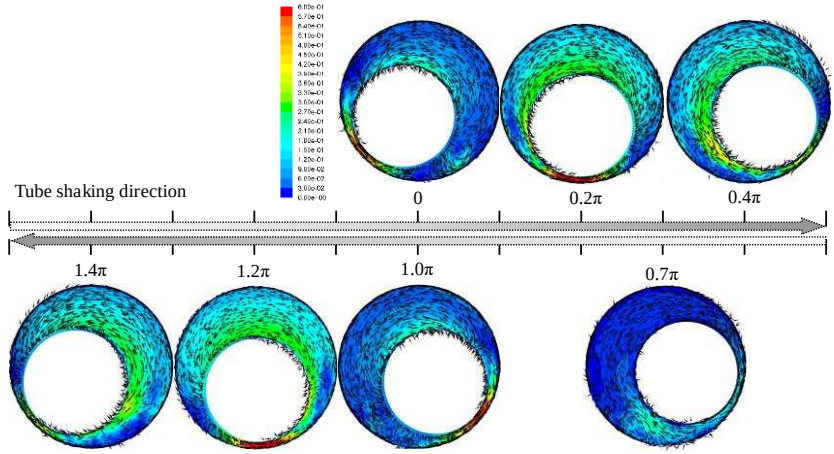

(b) Stress-BSL pressure-strain model

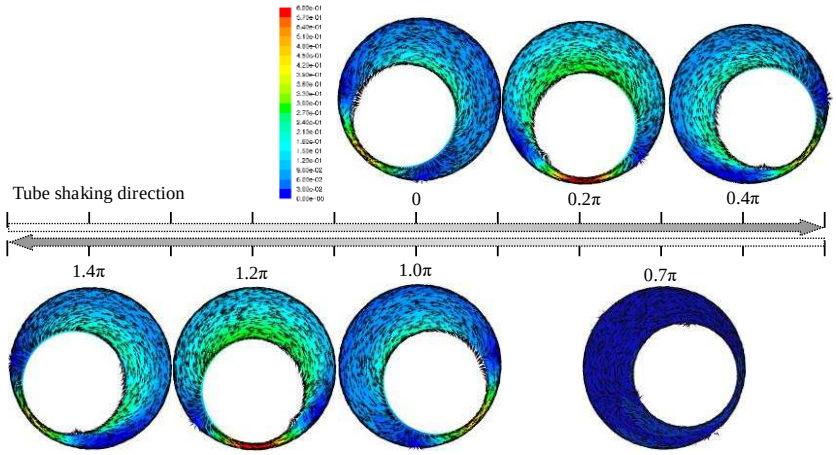

(c) Quadratic pressure-strain model

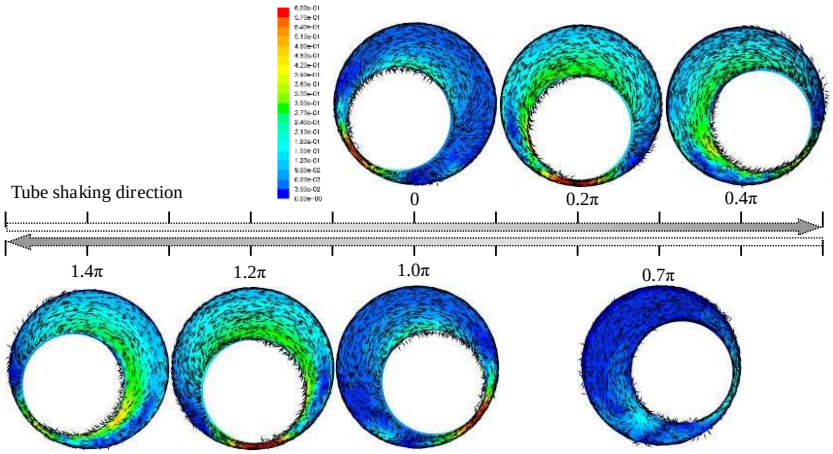

(d) Laminar flow model

Fig. 13. Velocities in the reference frame of the reactor tube obtained using different pressure-strain models in the RSM at phases A=0, B=0.2π, C=0.4π, D=0.7π, E = 1.0π, F = 1.2π and G =1.4π.

Instantaneous velocity vectors at different phases in the reference frame of the tube are also shown in Fig. 13. The dominant flow pattern is similar for all the models, with the fluid being pushed and divided into separated paths. The main difference lies in phase D where one large turbulent eddy is clearly shown at the lower left side of the agitator in the quadratic pressure-strain model predictions. Moreover, the quadratic pressure-strain model produced a more orderly flow than that of the other models. The irregularities seen in the fluid structure predicted by the other models are due to the flow in the axial direction. Additionally, the flow structures are predicted to be largely symmetrical by the quadratic pressure-strain model, as shown in phases A and E, when the agitator is located at the same height but at different sides of the tube.

In mixing devices, energy is mainly supplied to both the bulk flow and the regions with high shear rate. High levels of turbulence activity and high velocity gradients are often associated with regions of large turbulence kinetic energy. The turbulence structure thus plays an important role in determining the mixing capacity and the dominant mixing mechanism of the reactor. It is thus worthwhile to evaluate how the turbulence kinetic energy, k, evolves with time and how it is distributed within the ATR system. Fig. 14 shows the variation of the volume-averaged turbulence kinetic energy predicted by different pressure-strain models in the RSM. It can be observed that k

fluctuates in a periodic way for both the stress-BSL and the quadratic pressure-strain models. The quadratic pressure-strain model gives a consistently higher level (2.3-3 times larger) than that of the stress-BSL pressure-strain model. The turbulence kinetic energy peaks at around 0.5π and 1.5π which corresponds to the locations where the velocity of the tube vanishes. On the other hand, the stress-omega pressure-strain model yields essentially zero values, suggesting that this model is unable to capture the turbulence generated in the ATR system.

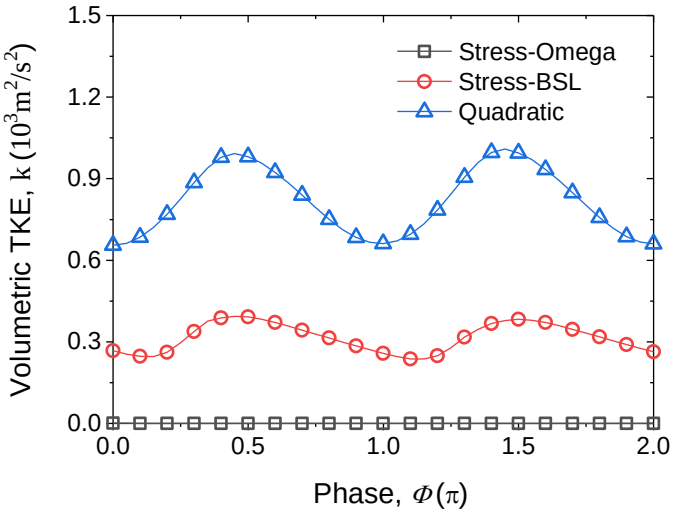

Fig. 14. Evolution of the volumetric turbulence kinetic energy by different pressure-strain models used in the RSM.

Fig. 15 shows the corresponding distribution of the turbulence kinetic energy in different phases. The stress-omega model failed to predict any turbulence in the ATR system at all stages, and hence is not included in this figure. The overall distributions of k predicted by the other two models are similar, with large values localized in front of the agitator when it moves towards the bottom of the reactor in phase A, and concentrated into the wake region in phase D. It should be noted that the distribution of k predicted by the quadratic pressure-strain model is wider and smoother than that of the stress-BSL pressure-strain model in which turbulence largely occurs in the contact region.

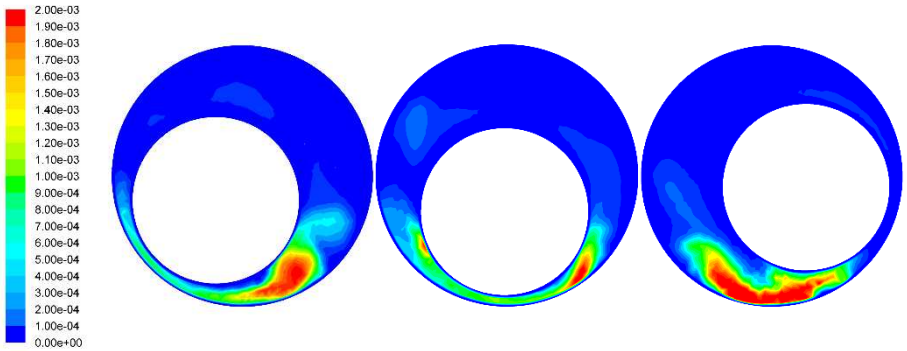

(a) Stress-BSL pressure-strain model

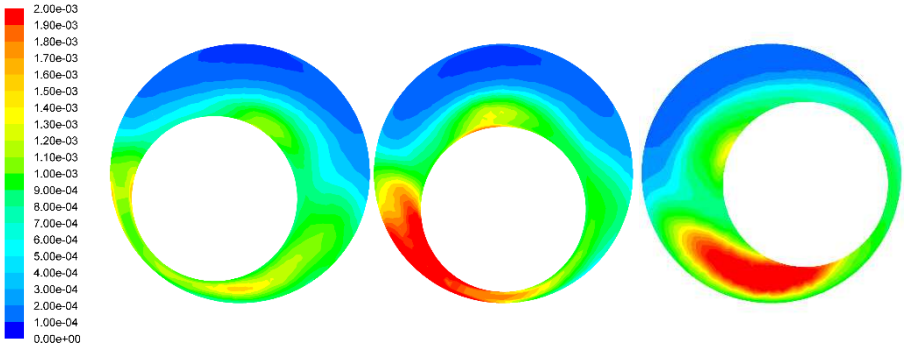

(b) Quadratic pressure-strain model

Fig. 15. Distribution of the turbulence kinetic energy using different pressure-strain models in the RSM in phase A=0, B=0.2π and D=0.7π.

Energy dissipation by turbulence is closely related to the flow structure at the microscale (Ng and Yianneskis, 2000). Knowledge of its magnitude and distribution is useful in understanding processes that depend on the degree of micro-mixing, such as the break-up of droplets and bubbles, chemical/biochemical reactions and particle dispersion. However, accurate determination of the dissipation rate is still challenging both computationally and experimentally, partly due to the small size of the dissipative scales that need to be resolved. Fig. 16 shows the distribution of the turbulence dissipation rate, ε, obtained by the different pressure-strain models (again excluding the stress-omega model as there was very little turbulence dissipation). For the other two models, the distribution of ε is very inhomogeneous, varying over a wide range of magnitudes. Results of the stress-BSL and the quadratic pressure-strain model are largely similar except that the latter model shows a smoother distribution of turbulence

dissipation than that of the stress-BSL model. This is in line with the distribution of the turbulence kinetic energy.

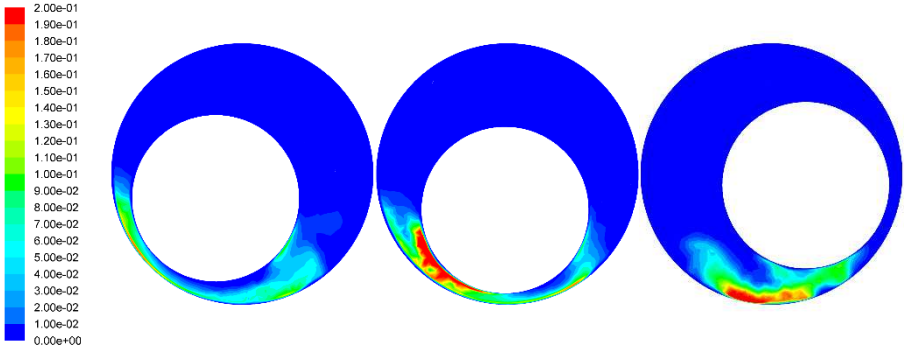

(a) stress-BSL pressure-strain model

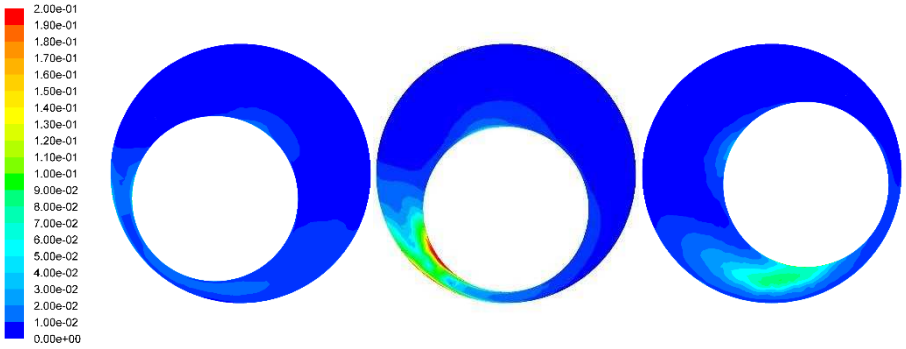

(b) Quadratic pressure-strain model

Fig. 16. Distribution of the turbulence energy dissipation rate using different pressure-strain models in the RSM in phase A=0, B=0.2π and D=0.7π.

4.5 Power consumption

The power input by the agitator is an important parameter for reactor design, affecting mixing and circulation time, and thus the performance of heat and mass transfer processes. The accurate estimation of power input is important for the scale-up, operation and optimization of reactor designs (Taghavi et al., 2011). For the ATR system, the power input only comes from the contribution of the agitator. The specific power consumption can be calculated as:

$$P/V = \frac{-\sum(\mathbf{F}\cdot\mathbf{v}+\mathbf{T}\cdot\boldsymbol{\omega})}{V} \tag{17}$$

where **v** is the translational velocity and **ω** the angular velocity of the agitator in the reference frame of the tube. **F** and **T** are the forces and torques due to the fluid flow, respectively.

The power consumption in the ATR system can be estimated from the energy dissipation in the fluid. There are two types of mechanism that lead to energy dissipation: turbulence dissipation and viscous dissipation. The volumetric energy dissipation rate can be estimated as:

$$\varepsilon = \int (\rho \varepsilon_t + \boldsymbol{\tau}\dot{\boldsymbol{\gamma}}) dV/V \tag{18}$$

where ε_t is the turbulence energy dissipation rate, τ the fluid stress and $\dot{\gamma}$ the fluid strain rate.

Fig. 17(a) shows the evolution of power input per volume predicted by the different pressure-strain models. The predicted power inputs are quite close for the two ω-based pressure-strain models, whilst the ε-based quadratic pressure-strain model predicts a slightly lower level than the other approaches. This likely due to the difference in predictions of the pressure force acting on the agitator, as shown in Fig. 12(a). It worth noting that the agitator does not always impart energy into the fluid, as evidenced by both the positive and negative values of the power. The negative work done by the agitator is mainly due to the reverse in the shaking direction of the tube. During this stage (0.4-0.6π and 1.4-1.6 π), the velocity of the tube is close to zero. Consequently, the agitator is no longer driven by the shaking tube, and its motion is increasingly affected by the fluid flow, thus leading to negative values of the power input.

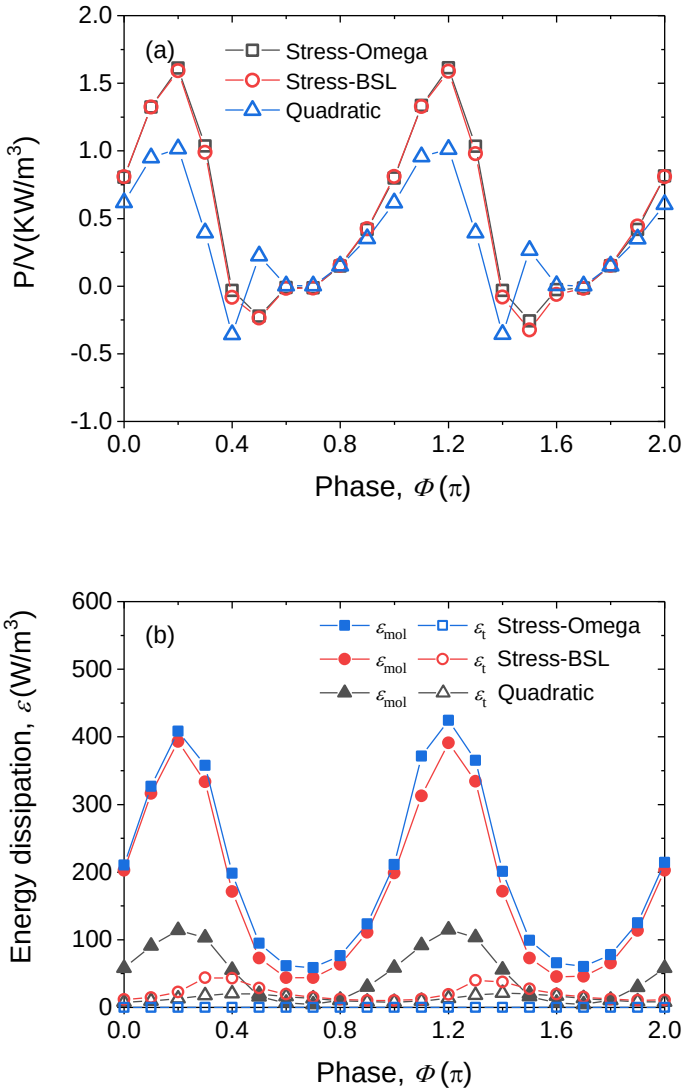

Fig. 17. (a) Power input and (b) power consumption per unit volume predicted by the different pressure-strain models in the RSM.

Fig. 17(b) shows the evolution of energy dissipation predicted by the different approaches. The levels of viscous dissipation predicted by the two ω-based pressure-strain models are comparable, and are consistently larger than those of the quadratic pressure-strain model. However, the highest level of turbulence dissipation was predicted by the stress-BSL pressure-strain model followed by the quadratic model. Essentially, no turbulence dissipation was predicted by the stress-omega model. It can be found that, for all the pressure-strain models, most of the energy is dissipated by viscous dissipation rather than by turbulence dissipation. This is contrary to what

occurs in most chemical reactors, such as stirred tanks, in which turbulence dissipation is the dominant mode of energy dissipation.

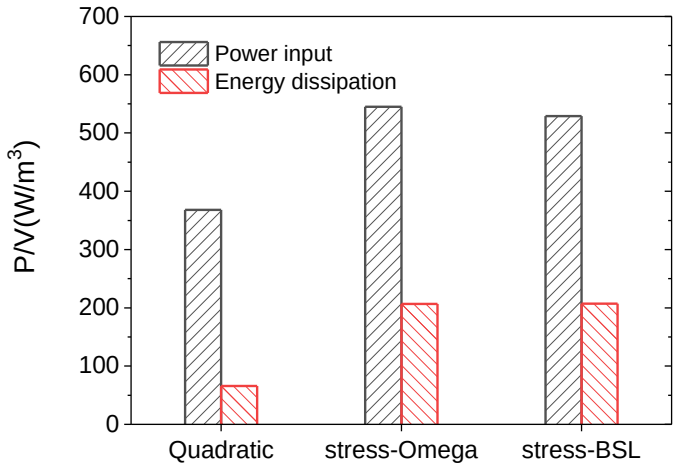

Fig. 18. Comparison of volumetric power input and power consumption.

Lastly, Fig. 18 compares the volumetric power input with the energy dissipation predicted by the different pressure-strain models used in the RSM. All the models adopted in the study appear to fail to predict enough energy dissipation. The reason for this is mainly due to the unresolved dissipative scales. High-order discretization schemes and scale-resolving methods, such as large eddy or direct numerical simulation, are expected to achieve better prediction of the power consumption. Relatively speaking, the stress-BSL and the stress-omega pressure-strain models appear more successful than the quadratic pressure-strain model (39% and 38%, versus 18%) in predicting power consumption in the ATR system. Considering the fact that the stress-omega pressure-strain model fails to predict any significant levels turbulence in the ATR system, while stress-BSL pressure-strain model predicts the highest levels of turbulence dissipation, further study using the stress-BSL model is recommended.

5. Conclusions

In this study, a new hybrid model to predict structure-structure and the fluid-structure interactions encountered in new designs of mechanically agitated tubular reactor was proposed. The proposed model combines a soft-sphere collision model, to resolve the interaction between structures, with a dynamic meshing approach, to couple the

motion of the moving structure with the fluid flow. The fluid forces and torques acting on the moving structure were calculated by integrating the pressure and viscous stress over its surface while dynamically re-meshing the computational domain to explicitly resolve the surrounding flow field. Compared to existing methods for FSI and SSI, the proposed CDDM approach is able to handle more complex geometries and to resolve boundary layer more accurately due to the use of body-conformal mesh, but at a cost of higher computational cost due to remeshing. The proposed model is fully incorporated into the CFD solver ANSYS Fluent through its user defined functions, thus enabling further extension to more general case studies.

The ability of the present model to handle FSI was demonstrated against literature data on the settling of a single sphere. The trajectories and velocities of the sphere during settling were well captured by the present model, showing quantitative agreement with experimental measurements. The flow structure around the sphere was also qualitatively captured, with an elongated wake present behind the sphere in the case of large Reynolds numbers. The energy consumption predicted by viscous dissipation was also in good agreement with the power input due to gravity, further confirming the validity of the present model in predicting fluid-structure interaction.

The developed model was further applied to the modelling of the ATR system. Sensitivity tests on grid resolution during dynamic meshing were conducted by varying the threshold of cell size, with no noticeable differences observed in terms of the dynamics of the agitator and the profile of fluid velocity at different phases of the agitator motion. Under lateral oscillation of the reactor tube, the internal agitator demonstrates a collision-dominated periodic movement pattern, yielding a maximum relative velocity of approximately 36.6% of that of the shaking tube. The agitated flow pattern varies between different phases of the inner tube oscillation, with vortex structures formed behind the agitator when it moves to its highest point. In addition, turbulence is also localized into the wake region of the agitator. Contrary to most large scale mixing devices, viscous dissipation was found to be the dominant mechanism for energy consumption in the ATR system.

The performance of three different pressure-strain models in the RSM was discussed. The pressure-strain model mainly affects the prediction of the viscous force due to

fluid flow. The ε-based quadratic model predicts the highest levels of turbulence kinetic energy when compared to the two ω-based pressure-strain models considered, with the stress-omega pressure-strain model failing to predict any significant levels of turbulence, highlighting the importance of accurate prediction in the near-wall region of the ATR system. Comparison between energy input and energy dissipation suggests an under-prediction of the energy consumption for all three pressure-strain models, although the stress-BSL pressure-strain model demonstrated the best performance when compared to the other two approaches. Further investigations using scale-resolving methods, such as large eddy or direct numerical simulation, have the potential to better capture the turbulence in the ATR system.

Acknowledgement

The authors would like to thank the European Commission for supporting this work as part of the research project "Intensified by Design® for the intensification of processes involving solids handling" under the H2020 SPIRE programme (SPIRE-08-2015-680565).

References

Abraham, F.F., 1970. Functional dependence of drag coefficient of a sphere on Reynolds number. Physics of Fluids 13, 2194-2195. https://doi.org/10.1063/1.1693218

Bakker, A., Van Den Akker, H.E.A., 1994. A computational model for the gas-liquid flow in stirred reactors. Chemical Engineering Research & Design 72, 594-606.

Balaras, E., 2004. Modeling complex boundaries using an external force field on fixed Cartesian grids in large-eddy simulations. Computers & Fluids 33, 375-404. https://doi.org/10.1016/S0045-7930(03)00058-6

Bathe, K.J., Zhang, H., Ji, S.H., 1999. Finite element analysis of fluid flows fully coupled with structural interactions. Computers & Structures 72, 1-16. https://doi.org/10.1016/S0045-7949(99)00042-5

Browne, D.L., Deadman, B.J., Ashe, R., Baxendale, I.R., Ley, S.V., 2011. Continuous flow processing of slurries: evaluation of an agitated cell reactor. Organic Process Research & Development 15, 693-697. https://doi.org/10.1021/op2000223

Brucato, A., Ciofalo, M., Grisafi, F., Micale, G., 1998. Numerical prediction of flow fields in baffled stirred vessels: a comparison of alternative modelling approaches. Chemical Engineering Science 53, 3653-3684. https://doi.org/10.1016/S0009-2509(98)00149-3

Cheng, Y.G., Oertel, H., Schenkel, T., 2005. Fluid-structure coupled CFD simulation of the left ventricular flow during filling phase. Annals of Biomedical Engineering 33, 567-576. https://doi.org/10.1007/s10439-005-4388-9

David, R., Marchal, P., Klein, J.P., Villermaux, J., 1991. Crystallization and precipitation engineering-III. A discrete formulation of the agglomeration rate of crystals in a crystallization process. Chemical Engineering Science 46, 205-213. https://doi.org/10.1016/0009-2509(91)80130-Q

Derksen, J.J., 2003. Numerical simulation of solids suspension in a stirred tank. AIChE Journal 49, 2700-2714. https://doi.org/10.1002/aic.690491104

Derksen, J.J., 2012. Highly resolved simulations of solids suspension in a small mixing tank. AIChE Journal 58, 3266-3278. https://doi.org/10.1002/aic.13889

Fadlun, E.A., Verzicco, R., Orlandi, P., Mohd-Yusof, J., 2000. Combined immersed-boundary finite-difference methods for three-dimensional complex flow simulations. Journal of Computational Physics 161, 35-60. https://doi.org/10.1006/jcph.2000.6484

Gasparini, G., Archer, I., Jones, E., Ashe, R., 2012. Scaling up biocatalysis reactions in flow reactors. Organic Process Research & Development 16, 1013-1016. https://doi.org/10.1021/op2003612

Hartmann, H., Derksen, J.J., van den Akker, H.E.A., 2006. Mixing times in a turbulent stirred tank by means of LES. AIChE Journal 52, 3696-3706. https://doi.org/10.1002/aic.10997

Harvey, A.P., Mackley, M.R., Seliger, T., 2003. Process intensification of biodiesel production using a continuous oscillatory flow reactor. Journal of Chemical Technology & Biotechnology: International Research in Process, Environmental & Clean Technology 78, 338-341. https://doi.org/10.1002/jctb.782

He, Y., Bayly, A.E., Hassanpour, A., 2018. Coupling CFD-DEM with dynamic meshing: A new approach for fluid-structure interaction in particle-fluid flows. Powder Technology 325, 620-631. https://doi.org/10.1016/j.powtec.2017.11.045

He, Y., Wang, Z., Evans, T.J., Yu, A.B., Yang, R.Y., 2015. DEM study of the mechanical strength of iron ore compacts. International Journal of Mineral Processing 142, 73-81. https://doi.org/10.1016/j.minpro.2015.05.005

He, Y., Evans, T.J., Yu, A.B., Yang, R.Y., 2018. A GPU-based DEM for modelling large scale powder compaction with wide size distributions. Powder Technology 333, 219-228. https://doi.org/10.1016/j.powtec.2018.04.034

Jaensson, N.O., Hulsen, M.A., Anderson, P.D., 2016. Direct numerical simulation of particle alignment in viscoelastic fluids. Journal of Non-Newtonian Fluid Mechanics 235, 125-142. https://doi.org/10.1016/j.jnnfm.2016.07.008

Jaisinghani, R., Ray, W.H., 1977. On The Dynamic Behavior of a class of homogeneous continuous stirred tank polymerization reactors. Chemical Engineering Science 32, 811-825. https://doi.org/10.1016/0009-2509(77)80067-5

Jones, E., McClean, K., Housden, S., Gasparini, G., Archer, I., 2012. Biocatalytic oxidase: batch to continuous. Chemical Engineering Research and Design 90, 726-731. https://doi.org/10.1016/j.cherd.2012.01.018

Kasat, G.R., Khopkar, A.R., Ranade, V.V., Pandita, A.B., 2008. CFD simulation of liquid-phase mixing in solid-liquid stirred reactor. Chemical Engineering Science 63, 3877-3885. https://doi.org/10.1016/j.ces.2008.04.018

Kerdouss, F., Bannari, A., Proulx, P., 2006. CFD modeling of gas dispersion and bubble size in a double turbine stirred tank. Chemical Engineering Science 61, 3313-3322. https://doi.org/10.1016/j.ces.2005.11.061

Kresta, S.M., Wood, P.E., 1991. Prediction of the three-dimensional turbulent flow in stirred tanks. AIChE journal 37, 448-460. https://doi.org/10.1002/aic.690370314

Mindlin, R.D., Deresiewicz, H., 1953. Elastic spheres in contact under varying oblique forces. Journal of Applied Mechanics-Transactions of the Asme 20, 327-344.

Ng, K., Yianneskis, M., 2000. Observations on the distribution of energy dissipation in stirred vessels. Chemical Engineering Research & Design 78, 334-341. https://doi.org/10.1205/026387600527446

Ni, X., Johnstone, J., Symes, K., Grey, B., Bennett, D., 2001. Suspension polymerization of acrylamide in an oscillatory baffled reactor: from drops to particles. AIChE journal 47, 1746-1757. https://doi.org/10.1002/aic.690470807

Pan, C.M., Min, J., Liu, X.H., Gao, Z.M., 2008. Investigation of fluid flow in a dual rushton impeller stirred tank using particle image velocimetry. Chinese Journal of Chemical Engineering 16, 693-699. https://doi.org/10.1016/S1004-9541(08)60142-1

Peskin, C.S., 1972. Flow patterns around heart valves: a numerical method. Journal of Computational Physics 10, 252-271. https://doi.org/10.1016/0021-9991(72)90065-4

Quirk, J.J., 1994. An alternative to unstructured grids for computing gas-dynamic flows around arbitrarily complex two-dimensional bodies. Computers & Fluids 23, 125-142. https://doi.org/10.1016/0045-7930(94)90031-0

Rutherford, K., Lee, K.C., Mahmoudi, S.M.S., Yianneskis, M., 1996. Hydrodynamic characteristics of dual Rushton impeller stirred vessels. AIChE Journal 42, 332-346. https://doi.org/10.1002/aic.690420204

Singh, K.K., Mahajani, S.M., Shenoy, K.T., Patwardhan, A.W., Ghosh, S.K., 2007. CFD modeling of pilot-scale pump-mixer: Single-phase head and power characteristics. Chemical Engineering Science 62, 1308-1322. https://doi.org/10.1016/j.ces.2006.10.028

Speziale, C.G., Sarkar, S., Gatski, T.B., 1991. Modeling the pressure strain correlation of turbulence: an invariant dynamic-systems approach. Journal of Fluid Mechanics 227, 245-272. https://doi.org/10.1017/S0022112091000101

Taghavi, M., Zadghaffari, R., Moghaddas, J., Moghaddas, Y., 2011. Experimental and CFD investigation of power consumption in a dual Rushton turbine stirred tank. Chemical Engineering Research and Design 89, 280-290. https://doi.org/10.1016/j.cherd.2010.07.006

ten Cate, A., Nieuwstad, C.H., Derksen, J.J., Van den Akker, H.E.A., 2002. Particle imaging velocimetry experiments and lattice-Boltzmann simulations on a single sphere settling under gravity. Physics of Fluids 14, 4012-4025. https://doi.org/10.1063/1.1512918

Tezduyar, T.E., Behr, M., Liou, J., 1992. A new strategy for finite-element computations involving moving boundaries and interfaces - the deforming-spatial-domain/space-time procedure .1. The concept and the preliminary numerical tests. Computer Methods in Applied Mechanics and Engineering 94, 339-351. https://doi.org/10.1016/0045-7825(92)90059-S

Udaykumar, H.S., Shyy, W., Rao, M.M., 1996. ELAFINT: A mixed Eulerian-Lagrangian method for fluid flows with complex and moving boundaries. International Journal for Numerical Methods in Fluids 22, 691-712. https://doi.org/10.1002/(SICI)1097-0363(19960430)22:8<691::AID-FLD371>3.0.CO;2-U

Villone, M.M., D'Avino, G., Hulsen, M.A., Greco, F., Maffettone, P.L., 2011. Numerical simulations of particle migration in a viscoelastic fluid subjected to Poiseuille flow. Computers & Fluids 42, 82-91. https://doi.org/10.1016/j.compfluid.2010.11.009

Wilcox, D.C., 1998. Turbulence modeling for CFD. DCW industries La Canada, CA.

Zadghaffari, R., Moghaddas, J.S., Revstedt, J., 2009. A mixing study in a double-Rushton stirred tank. Computers & Chemical Engineering 33, 1240-1246. https://doi.org/10.1016/j.compchemeng.2009.01.017

Zhou, Y.C., Wright, B.D., Yang, R.Y., Xu, B.H., Yu, A.B., 1999. Rolling friction in the dynamic simulation of sandpile formation. Physica A 269, 536-553. https://doi.org/10.1016/S0378-4371(99)00183-1

Zhu, H., Zhou, Z., Yang, R., Yu, A., 2007. Discrete particle simulation of particulate systems: theoretical developments. Chemical Engineering Science 62, 3378-3396. https://doi.org/10.1016/j.ces.2006.12.089